JACS
JOURNAL OF THE AMERICAN CHEMICAL SOCIETY

Article

pubs.acs.org/JACS

Evolution of Physical and Electronic Structures of Bilayer Graphene upon Chemical Functionalization

Qing Hua Wang, Chih-Jen Shih, Geraldine L. C. Paulus, and Michael S. Strano*

Department of Chemical Engineering, Massachusetts Institute of Technology, Cambridge, Massachusetts 02139, United States

Supporting Information

ABSTRACT: The chemical behavior of bilayer graphene under strong covalent and noncovalent functionalization is relatively unknown compared to monolayer graphene, which has been far more widely studied. Bilayer graphene is significantly less chemically reactive than monolayer graphene, making it more challenging to study its chemistry in detail. However, bilayer graphene is increasingly attractive for electronic applications rather than monolayer graphene because of its electric-field-controllable band gap, and there is a need for a greater understanding of its chemical functionalization. In this paper, we study the covalent and noncovalent functionalization of bilayer graphene using an electrochemical process with aryl diazonium salts in the high conversion regime (D/G ratio >1), and we use Raman spectroscopic mapping and conductive atomic force microscopy (cAFM) to study the resulting changes in the physical and electronic structures. Covalent functionalization at high chemical conversion induces distinct changes in the Raman spectrum of bilayer graphene including the broadening and shift in position of the split G peak. Also, the D peak becomes active with four components. We report for the first time that the broadening of the $2D_{22}$ and $2D_{21}$ components is a distinct indicator of covalent functionalization, whereas the decrease in intensity of the $2D_{11}$ and $2D_{12}$ peaks corresponds to doping. Conductive AFM imaging shows physisorbed species from noncovalent functionalization can be removed by mechanical and electrical influence from the AFM tip, and that changes in conductivity due to functionalization are inhomogeneous. These results allow one to distinguish covalent from noncovalent chemistry as a guide for further studies of the chemistry of bilayer graphene.

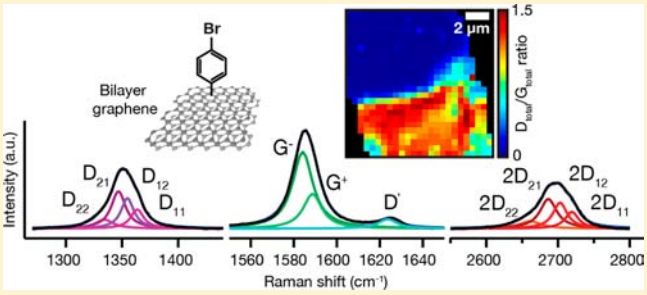

INTRODUCTION

In the past several years, graphene has rapidly emerged as an important material in electronics because of its quantum electronic properties, exceptionally high mobilities, and large-scale processability.[1−3] The chemical functionalization of graphene has been extensively studied for monolayer graphene (MLG) by a variety of covalent[4−7] and noncovalent[8,9] routes in order to change its doping level and electronic structure, as well as to change its chemical properties[3,8] and incorporate graphene with other molecular components[10] such as polymers and make it suitable for organic photovoltaics.[11] Many fascinating results have been observed in studies of the chemistry of graphene. For example, our laboratory first showed that monolayer graphene has anomalously high chemical reactivity, much higher than that of bilayer graphene (BLG), and that graphene edges have preferential reactivity.[12] We also showed recently that electron transfer chemistries of graphene are strongly influenced by the underlying substrate.[13]

Many of the motivations for studying the chemical functionalization of monolayer graphene also apply to bilayer graphene. Bilayer graphene has attracted increasing interest[14−16] because in contrast to monolayer graphene, which lacks a band gap and requires complex strategies[6,17−25] to modify its transport properties to overcome its insufficiently low "off"-state current as a transistor,[6,26] its electronic structure features parabolic rather than linear bands,[27] resulting in an electric-field-controllable band gap.[28,29] The band gap can also be controlled by chemical functionalization or doping on the top and bottom surfaces to generate an external electric field without the use of electrostatic gating.[16,30,31] However, the chemistry of bilayer graphene has been much less extensively studied compared to monolayer graphene and, as a result, its chemistry is far less understood. This discrepancy is partly because bilayer graphene is far less reactive than monolayer graphene, as our group[12] and others[32] have shown, making it much more difficult to study in detail at high degrees of functionalization. There is a need to study the chemical functionalization of bilayer graphene by both covalent and noncovalent routes in much more detail.

In this paper, we present a detailed Raman spectroscopic and conductive atomic force microscopy (AFM) study of the covalent chemical functionalization of bilayer graphene by aryl diazonium salts and investigate the structural and electronic changes that occur with increasing functionalization. We use an electrochemical functionalization method, which allows for a

Received: August 13, 2013
Published: November 22, 2013

   dx.doi.org/10.1021/ja4083914 | J. Am. Chem. Soc. 2013, 135, 18866−18875

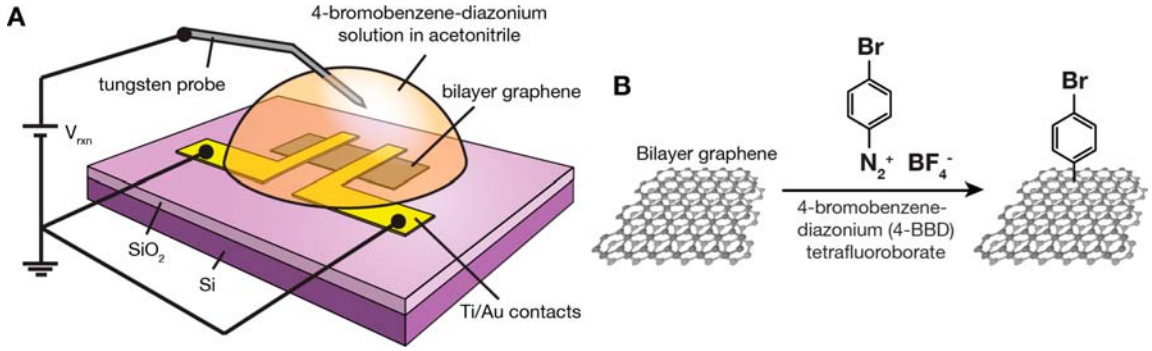

Figure 1. Covalent electrochemical functionalization of bilayer graphene. (A) Schematic of experimental setup. Bilayer graphene from mechanical exfoliation is deposited on SiO_2/Si wafer and connected by Ti/Au metal contacts to ground. A droplet of 4-bromobenzene-diazonium (4-BBD) tetrafluoroborate solution in acetonitrile covers the bilayer flake. A tungsten probe inserted into the solution droplet applies a bias voltage during reaction, V_{rxn}. (B) Reaction scheme for covalent functionalization of 4-BBD on bilayer graphene.

much greater degree of covalent attachment than without application of a bias voltage as we have shown previously.[19] After each successive functionalization step, resulting in an increasing density of covalent reaction sites on the graphene lattice, we evaluate Raman spectra and study the evolution of structural and electronic properties of bilayer graphene. We also contrast the covalently functionalized bilayer graphene to portions of the same sample that are not electrochemically gated and are therefore only noncovalently functionalized. Finally, we also show conductive atomic force microscopy (cAFM) imaging of both covalently and noncovalently functionalized bilayer graphene. During contact mode conductive AFM imaging, mechanical and electrical cleaning of the samples occurs, causing removal of physisorbed layers that have deposited in the noncovalent component of the diazonium functionalization. Conductive AFM imaging also shows spatial inhomogeneity of the conductivity of the bilayer regions after functionalization. Our results are important for further understanding the chemistry of bilayer graphene, and we also provide a set of spectroscopic markers for distinguishing covalent and noncovalent chemical functionalization of bilayer graphene that will be valuable to the graphene community to guide further studies.

RESULTS AND DISCUSSION

Electrochemical Functionalization. The covalent functionalization of graphene with diazonium salts has been extensively studied previously (see ref 6 and references therein). The reaction mechanism involves the transfer of an electron from the substrate (graphene) to the aryl diazonium cation, which becomes a highly reactive aryl radical upon release of a nitrogen molecule. This radical then rapidly forms a covalent bond with the graphene lattice (Figure 1B), changing the hybridization of the carbon atom at the covalent attachment site from sp^2 to sp^3. Because the rate-limiting step is the initial electron transfer step, the overlap in the density of states of the graphene and the aryl diazonium molecule determines the reaction kinetics and selectivity.[6,12] The reactivity of bilayer graphene under nonelectrochemical conditions has been shown to be far lower than that of monolayer graphene in opposition to conventional electron transfer theory.[12,32] Our revised theory describes this as the decreased influence of electron-rich puddles due to charged impurities in the substrate,[13] which locally shift the Fermi level to positions of significant overlap of states between the graphene and diazonium molecule for monolayer graphene. However, this effect is suppressed in bilayer graphene because the bottom layer of graphene screens the effect of the charged impurities,[12,13] leading to far lower reactivity for bilayer than monolayer graphene.[12,32] In our previous work, we have shown that shifting the Fermi level by applying an external bottom gate bias can significantly increase the reaction rate.[13] Similarly, by applying a bias voltage to a metal probe inserted into a droplet of aryl diazonium ions in solution covering the sample the reactivity is greatly accelerated by (1) shifting the Fermi level of the graphene and (2) increasing the concentration of diazonium ions at the graphene surface.[13,19] Because of the latter, the degree of noncovalent functionalization with physisorbed species is also increased when a bias is applied. In the present work, we are able to study the effect of a high degree of covalent functionalization of bilayer graphene using the electrochemical functionalization method.

Bilayer graphene flakes were prepared by mechanical exfoliation onto 300 nm SiO_2/Si wafers and identified by optical microscopy. Electrical contacts were fabricated by photolithography and deposition of Ti/Au electrodes. The schematic of the sample, contacts, and electrochemical functionalization geometry is shown in Figure 1A, with more details in the Methods and Materials section below. During each reaction step, a reaction voltage V_{rxn} is applied to a tungsten probe inserted into the solution droplet for 1 min, and the electrodes in contact with the bilayer graphene flake are grounded. The reagent solution was 4-bromobenzene-diazonium tetrafluoroborate in acetonitrile, which reacts covalently with the graphene lattice as shown in Figure 1B. In our experiments, we characterized the sample using Raman spectroscopy after each of three successive reaction steps of 1 min each: reaction 1, V_{rxn} = 1.0 V; reaction 2, V_{rxn} = 1.25 V; and reaction 3, V_{rxn} = 1.5 V. After each reaction step, the sample was thoroughly rinsed in acetonitrile and blown dry with ultrapure nitrogen before conducting Raman spectroscopy.

A bilayer sample contacted by two Ti/Au electrodes is shown in the optical microscope image of Figure 2C, and a magnified image of the region in the dashed square is shown in Figure 2D. There is a fracture across the bilayer graphene flake at the location of the curved dotted line, such that the region of the flake above the fracture is not in electrical contact with the Ti/Au electrodes and is not subjected to the same electrochemical functionalization. This upper region can still undergo the covalent functionalization, albeit at a much lower rate as we have shown in our previous work.[12] It is labeled "Non-cov." to

dx.doi.org/10.1021/ja4083914 | J. Am. Chem. Soc. 2013, 135, 18866−18875

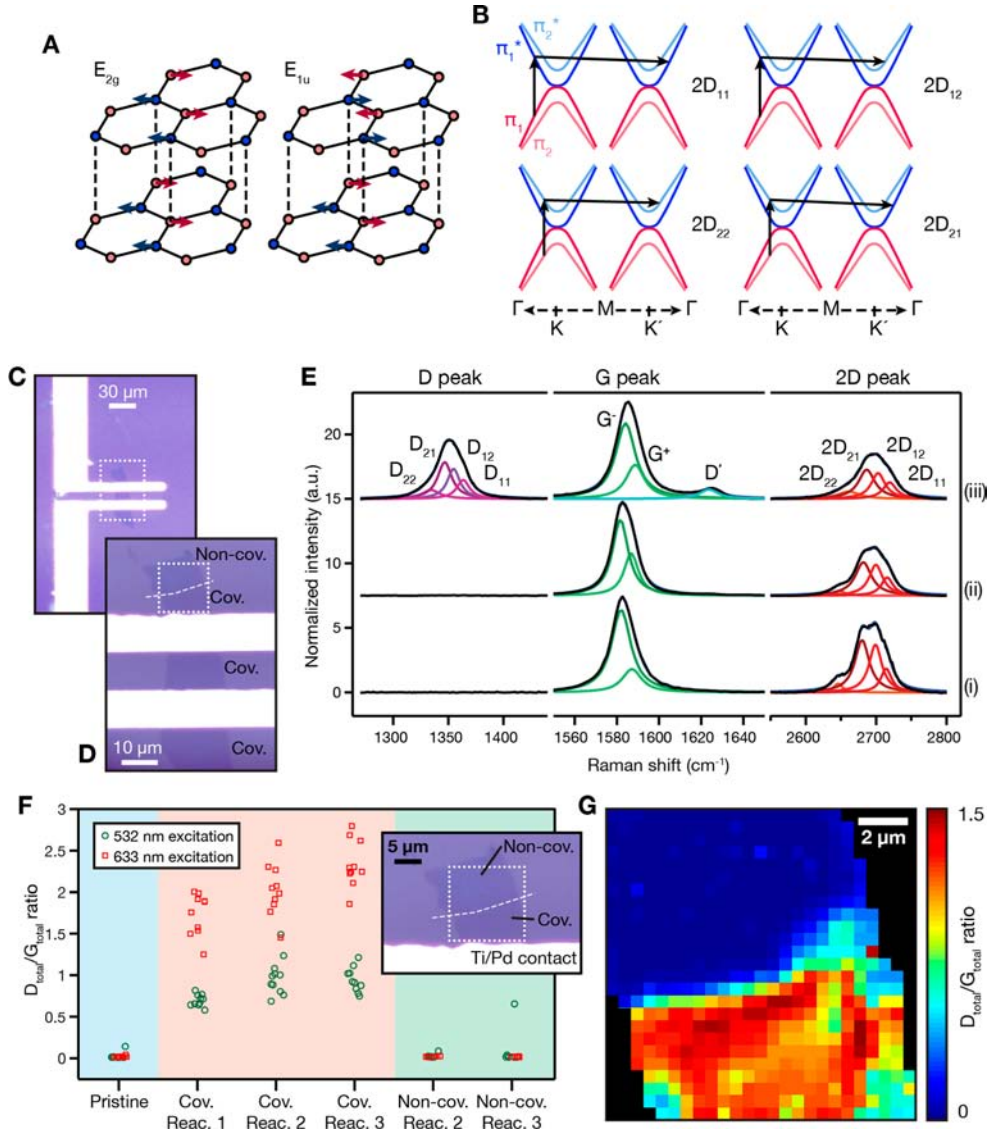

Figure 2. Raman spectroscopy of functionalized bilayer graphene. (A) Atomic displacements for phonons that contribute to the G peak: E_{2g} (in phase, Raman-active), E_{1u} (out of phase, IR-active unless symmetry is broken). Adapted from Ferrari et al.[35] (B) Electronic band diagram of bilayer graphene near the K and K′ points showing the four allowed double resonance (DR) transitions that contribute to the 2D peak. Adapted from Malard et al.[36] (C) Optical microscope image of a bilayer graphene flake. The bright rectangular regions are the Ti/Au metal contacts. (D) Magnified optical microscope image of the region in the dotted rectangle in part C. This particular bilayer graphene sample had a fracture along the dashed line, so that the regions in electrical contact with the Ti/Au contacts become predominantly covalently functionalized. The disconnected region above the fracture is primarily noncovalently functionalized. (E) Representative Raman spectra of (i) unfunctionalized bilayer graphene after device fabrication, (ii) bilayer graphene in the disconnected region after three reactions, showing only noncovalent functionalization, and (iii) bilayer region in the connected region between two contacts after three reactions, showing significant covalent reaction as evidenced by the appearance of the D peak and D′ peak. The D peak for bilayer graphene here shows four Lorentzian components due to the interaction with the electronic structure. In all spectra, the Lorentzian fit components are shown. All spectra are normalized to the height of the G peak maximum. All spectra in (E) were obtained with 532 nm excitation. (F) Ratios of total D peak intensity (area of all 4 components) and total G peak intensity (area of G^+ and G^- components) for pristine graphene after device fabrication (blue shaded region), covalently reacted bilayer graphene (red shaded region), and noncovalently reacted (green shaded region), corresponding to the regions marked "Cov." and "Noncov." in part D. Data are shown for both 532 and 633 nm excitation. (G) Spatial map of total D peak intensity (4 components) divided by total G peak intensity (2 components) in the dotted square marked in part D, with Raman spectra taken at 532 nm excitation.

indicate that it primarily undergoes noncovalent functionalization, whereas the other regions of the sample that are in contact are labeled "Cov." because they undergo significant covalent functionalization due to the applied bias voltage. Previous reports have shown that graphene under differing reaction conditions can result in a mixture of covalent and noncovalent functionalization with diazonium salts, including covalently attached and noncovalently physisorbed monomers and oligomers.[6,33,34] In the present work, using bilayer graphene flakes that have regions undergoing both electrochemical and nonelectrochemical functionalization, we can simultaneously generate the covalent and noncovalent contributions and characterize them in the same sample. This comparison, studied here for the first time, has utility in understanding the chemistry of bilayer graphene, as it allows one to use

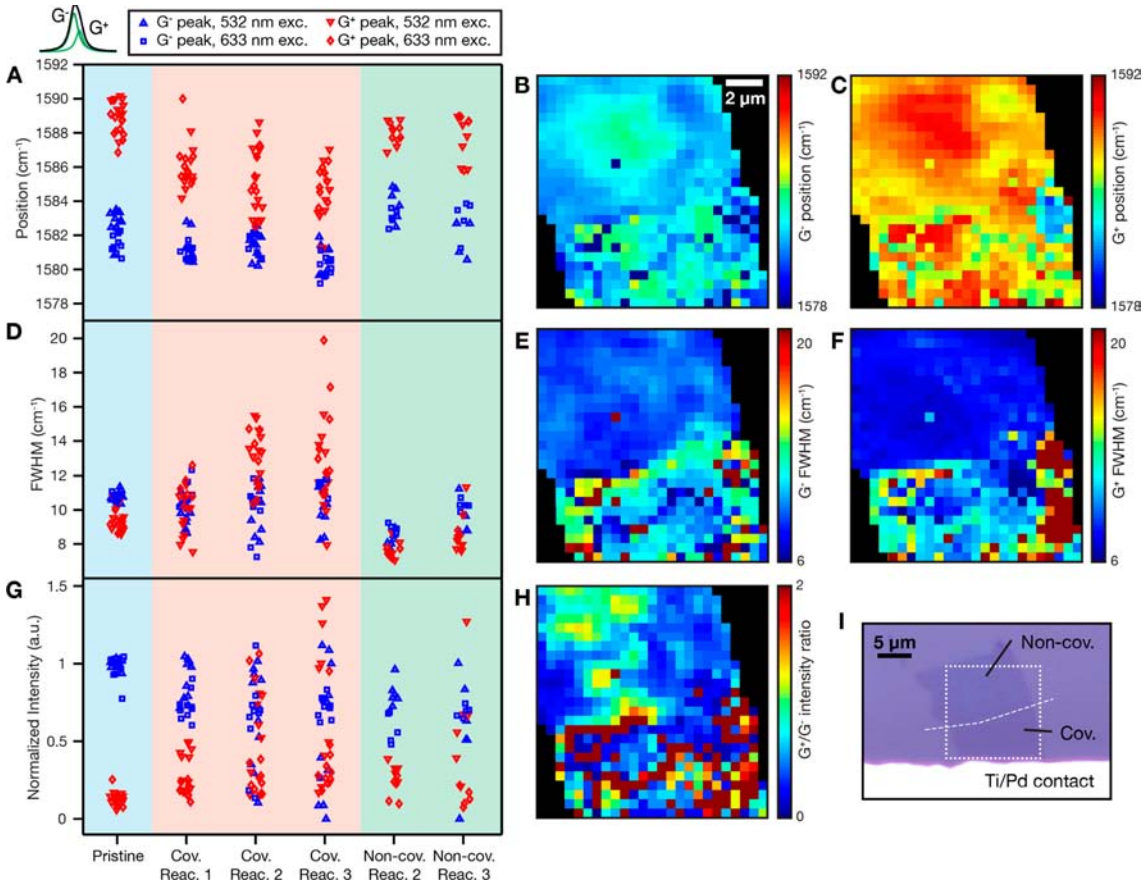

Figure 3. Evolution of Raman G peak with increasing functionalization. (A), (D), (G) The peak parameters of the G^+ and G^- peaks are plotted on the *y* axis as a function of reaction on the *x* axis. Data from the pristine samples before any reaction are in the first column (blue shading), data from after each successive reaction in the portion of the sample connected to the electrode are in the next three columns (pink shading), and data from the portion of the sample not connected to the electrode are in the final two columns (green shading). The data for the G^+ peaks are the red points, and the G^- peaks the blue points. The peak parameters are (A) the position, (D) full width at half-maximum (FWHM), and (G) normalized peak intensity (area). Spatial Raman maps of the (B) G^+ and (C) G^- peak positions and (E and F) FWHMs and (H) the G^+/G^- intensity ratio. All Raman spectra for the spatial maps were taken using 532 nm excitation. (I) Optical image of the sample, with the region in the dotted square shown in all the Raman spatial maps.

spectroscopy to deconvolute and understand these two reaction pathways.

Raman spectroscopy. Raman spectroscopy is one of the most important characterization tools in studying graphene because it provides information on the electronic, structural, chemical, and mechanical properties of graphene quickly and nondestructively.[35,36] Representative Raman spectra of the bilayer graphene sample (i) before and (ii–iii) after all three reaction cycles are shown in Figure 2E. The main features of the Raman spectrum of bilayer graphene that we will discuss are the G peak near 1580 cm^{-1}, the D peak near 1350 cm^{-1}, and the 2D peak near 2650 cm^{-1}. The G peak arises from the E_{2g} phonon at the Γ point, and in bilayer graphene, the symmetry breaking and intermixing of in-phase (E_{2g}) and out-of-phase (E_{1u}) in-plane phonons[35,37] results in the G peak splitting into G^+ and G^- peaks with higher and lower wavenumber positions, respectively.[37] The atomic movements in bilayer graphene contributing to these phonons are shown in Figure 2A. The Raman spectra in Figure 2E show these G^+ and G^- components. The relative positions, widths, and intensities of the G^+ and G^- peaks have been shown to indicate the degree of doping of bilayer graphene,[37−39] and will be analyzed in more detail below.

The 2D peak is a two-phonon symmetry-allowed mode that is dispersive, and is routinely used to identify and distinguish monolayer and bilayer graphene from graphite. Because it arises because of an intervalley double-resonance (DR) Raman process that involves both electronic states and phonons[40−42] and because bilayer graphene features a split of the valence and conduction bands into two parabolic branches near the K-point, there are four allowed intervalley DR processes,[42,43] resulting in four peaks in the 2D peak.[38,39,41] These peaks are labeled $2D_{22}$, $2D_{21}$, $2D_{12}$, and $2D_{11}$ according to the transitions at the K and K′ points of bilayer graphene, as shown in Figure 2B. We can see in all three spectra in Figure 2E that the 2D peak consists of these four transitions.

The D peak is a symmetry-disallowed two-phonon mode and is only seen when there are symmetry-breaking defects in the graphene lattice. In monolayer graphene, the D band is a single peak, but in bilayer graphene, it has been shown to split into four peaks.[19,44] The pristine bilayer graphene spectrum in (i) shows no D peak, indicating that the sample is pristine without a detectable concentration of initial defects. The spectrum in (ii) corresponds to the detached region (Non-cov.) after three reaction steps. Because this region of the sample is not connected to the electrical contacts, the Fermi level is not shifted when the reaction bias is applied, and covalent reaction

dx.doi.org/10.1021/ja4083914 | J. Am. Chem. Soc. 2013, 135, 18866−18875

occurs much more slowly. As a result, there is still no D peak. However, there is a change in the G^+ and G^- positions, widths, and relative intensities, indicating a change in doping, which is discussed in more detail below. However, in spectrum (iii), a prominent D peak has appeared, indicating covalent reaction sites. Because the 2D peak is the overtone of the D peak, in turn, the D peak for bilayer graphene can also be deconvolved into four Lorentzian components. These are labeled, by analogy to the 2D components, as D_{22}, D_{21}, D_{12}, and D_{11}.

In our lab's earliest work with bilayer graphene and diazonium chemistry,[12] and that of others,[32] the degree of covalent reaction was insufficient to generate a high enough D peak to resolve the four components. In our more recent work with bilayer graphene,[19] we covalently functionalized bilayer graphene to much higher concentrations using the same electrochemical bias method used in the present paper, and we showed for the first time to our knowledge that a highly chemically functionalized bilayer graphene has a four-component D-peak. An earlier contribution from Jorio et al. showed that bilayer graphene damaged by ion bombardment has a similar four-component D-peak.[44]

To assess the degree of covalent functionalization, we calculated the intensity ratio of the total D peak area (four components) to the total G peak area (two components), $I(D_{total})/I(G_{total})$, as a function of reaction step (Figure 2D). We use the area ratio rather than the height because the D peak has a complex shape, and the area of the peak is a better measure of the total probability of the Raman transitions. This area intensity ratio, corresponding to the concentration of covalent reaction sites, increases and begins to saturate for the attached bilayer region (Cov. region), but remains at zero for the detached bilayer (Non-cov. region). We note that there is a difference in D peak intensity with excitation wavelength; a similar effect has been previously reported for monolayer graphene and is likely due to a combination of electron/hole and phonon scattering efficiencies and optical interference effects.[45]

A spatial map of the $I(D_{total})/I(G_{total})$ ratio after reaction 3 in a 10 μm × 10 μm area of the sample is shown in Figure 2E, with the upper detached region showing a uniformly low ratio and the lower attached region showing much higher values, consistent with the plot in Figure 2D. In this map, there is noticeable spatial inhomogeneity even though the graphene flake is a single crystal with uniform structure. There is likely an influence of the underlying substrate on the measured Raman features, as we have shown in our previous work, contributing to the spatial inhomogeneity.[13] We also note that there is no preference for increased reaction at the edges, which was observed in previous papers with conventional aryl diazonium chemistry without applying a bias voltage.[12,32] Instead, we believe that the effect of the bias voltage overwhelms the effect of edge disorder in the chemical reactivity, which we have previously reported.[19]

The evolution of the G peak with an increasing degree of functionalization is shown in Figure 3. The scatter plots in Figures 3A, 3D, and 3G show the changes in the positions, full widths at half-maximum (FWHMs), and normalized intensities of the G^+ and G^- peak components after each reaction step, in both the attached and detached portions of the sample. Spatial maps of these peak parameters are also shown in Figure 3 panels B, C, E, F, and H.

In Figure 3A, the G^+ and G^- peak positions both are shown to downshift slightly with increasing covalent functionalization. However, the G^- peak seems to upshift slightly for noncovalent functionalization, relative to pristine graphene, which we interpret as doping of the graphene. The dependence of the G^+ and G^- peak positions on Fermi level alone in bilayer graphene have been theoretically calculated[46] and experimentally measured[37] in a top-gated transistor device. The explanation of these G-peak shifts can be rather complicated with the added chemistry. We now show that the G^+ and G^- peaks also change in peak position with effective doping from both covalent and noncovalent chemical functionalization. In particular, the downshift of the peaks under covalent functionalization cannot be explained with doping alone and appears to be a feature of covalent functionalization. The amount of peak position shifting from chemistry alone is rather small compared to the high degree of doping shown by Yan et al. using electrostatic gating.[37] The spatial maps of G^+ and G^- peak positions in Figures 3B and 3C show small patches in the shifts of the peak positions within the covalent section, but the noncovalent section features lower values around the edges and higher values in the center. Because the peaks downshift for increasing noncovalent functionalization as well, as shown in Figure 3A, this observation suggests a higher degree of doping at the edges. Previous work has shown that higher reactivity at the edges of graphene occurs with diazonium functionalization in the absence of an applied electric field[12,32] but does not persist when there is an applied electric field, as mentioned earlier.[19] However, it is possible that there is a small amount of covalent functionalization at the more reactive edges that is not high enough to activate a visible D peak.

The FWHMs of the G^+ and G^- peaks are shown in Figures 3D–F. The G^+ peak broadens significantly for increasing covalent functionalization in some spectra, but because of the spatial inhomogeneity of the reaction, there are some spectra in which it does not broaden, resulting in a scattered distribution of widths in Figure 3D. The G^- peak does not significantly change in width. In noncovalent functionalization, there is no significant broadening observed. In monolayer graphene that has been rendered disordered by chemistry or ion bombardment, there is broadening of the G peak.[47−49] Changes in electron−phonon coupling in monolayer graphene can also affect the width of the G peak.[50−52] We expect that there is a combination of effects in our experimental data: both the presence of disorder within and charge on top of the upper layer of bilayer graphene affects the phonon modes and electron−phonon coupling. However, in the work of Yan et al.,[37] the G^+ peak does not broaden across a wide range of Fermi levels, so it is more likely that we are seeing an effect of disorder in the observed broadening of the G^+ peak. Distortion of the carbon lattice and of the spacing between graphene layers because of covalent functionalization may also contribute to peak broadening because the G peak corresponds to in-plane phonon modes. We also note that local fluctuations of the Fermi level in space as a result of inhomogeneous doping with functionalization can also contribute to inhomogeneous broadening of the peak.

The relative changes in the area intensities of the G^+ and G^- peaks are shown in Figures 3G–H normalized to the average G^- peak intensity of pristine bilayer graphene. The G^- peak tends to decrease in intensity and the G^+ peak tends to increase in intensity with increasing functionalization. However, the distribution of intensities for both peaks also broadens such that there is a wide range of intensities seen at high functionalization. This distribution can be directly visualized

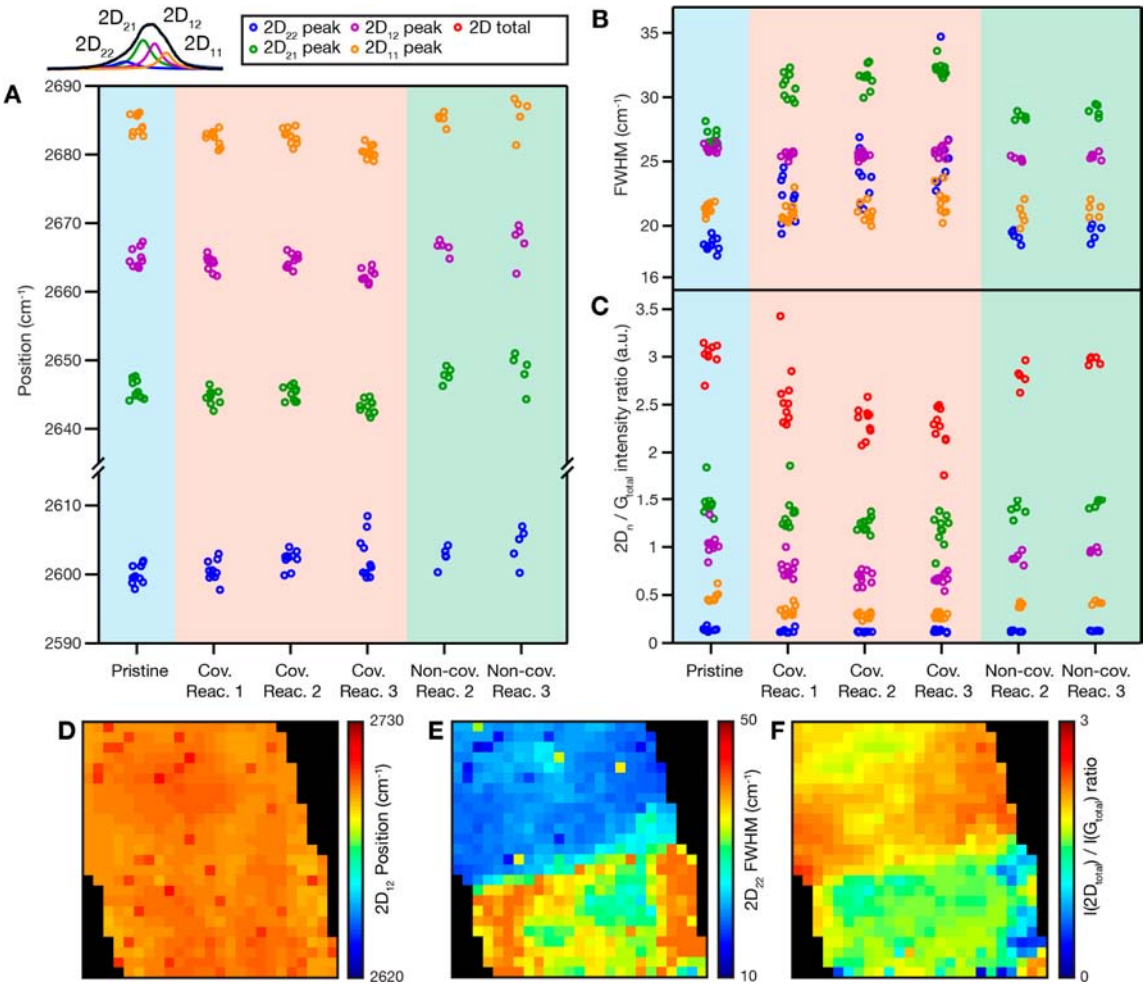

Figure 4. Evolution of Raman 2D peak with reaction. (A)−(C) Peak parameters of the 2D peak's four components are plotted on the *y* axis as a function of reaction on the *x* axis. Similar to Figure 3, data from the pristine samples before any reaction are in the first column (blue shading), data from after each successive reaction in the portion of the sample connected to the electrode are in the next three columns (pink shading), data from and the portion of the sample not connected to the electrode are in the final two columns (green shading). The data points for each of the four components are indicated by a different color: blue for $2D_{22}$, green for $2D_{21}$, purple for $2D_{12}$, and orange for $2D_{11}$. The peak parameters plotted are (A) position, (B) FWHM, and (C) ratio of the given peak area to the total area of the G peak (sum of G^+ and G^-). For clarity, only the data from Raman spectra taken with 633 nm excitation are shown in panels (A)−(C); very similar equivalent data at 532 nm excitation are shown in the Supporting Information, Figure S1. (D)−(F) Spatial Raman maps of (D) $2D_{12}$ position, (E) $2D_{22}$ FWHM, and (F) ratio of the total 2D area intensity to the total G area intensity from Raman spectra taken with 532 nm excitation. For clarity, only these three maps are shown; maps of all peak parameters are shown in the Supporting Information, Figure S2. Confidence intervals for the fitting parameters of the 2D peak are shown in the Supporting Information, Figure S3.

in the spatial map of Figure 3H as a high degree of spatial inhomogeneity. The changes in intensities in the noncovalent region are attributed to doping due to physisorption, whereas those in the covalent region also have a contribution from the formation of covalent attachment sites, which tend to be p-doping due to the withdrawal of an electron.[6,13] The changes in relative intensities were also reported at different Fermi levels by Yan et al.,[37] indicating phonon mixing and symmetry breaking with doping, so the spatial inhomogeneity in our data shows that the chemical functionalization is nonuniform in space. The origins of the spatial inhomogeneity of chemical functionalization are not clear, but some likely contributing factors include spatial variations in the Fermi level due to the substrate[13] and residues from photolithography.

The evolution of the 2D peak with an increasing degree of functionalization is shown in Figure 4. The confidence intervals of peak fitting for the four Lorentzians used to fit the 2D peak are shown in the Supporting Information, Figure S3. Previous studies have demonstrated that changes in the Fermi level (i.e., doping) of bilayer graphene result in changes in the G peak components[37−39,53] and 2D peak components.[54] However, these earlier works have focused on doping alone via electrostatic gating and have not shown the effect of chemical functionalization. Also, Martins Ferreira et al. have shown some observations of the 2D peak components with disorder due to ion bombardment, but not at significant detail and not for covalent functionalization.[44] The positions of each of the four components is shown in Figure 4A, the FWHMs in Figure 4B, and the intensity ratio with respect to the total G area intensity in Figure 4C. With increasing covalent functionalization, the $2D_{22}$ peak upshifts slightly, whereas the other three peaks downshift slightly. The spatial map for the $2D_{12}$ peak in Figure 4D shows that the variation in peak positions is not dramatically noticeable between the covalent and noncovalent regions and that there is some spatial fluctuation across the sample between the edges and the centers, similar to what was

dx.doi.org/10.1021/ja4083914 | J. Am. Chem. Soc. 2013, 135, 18866−18875

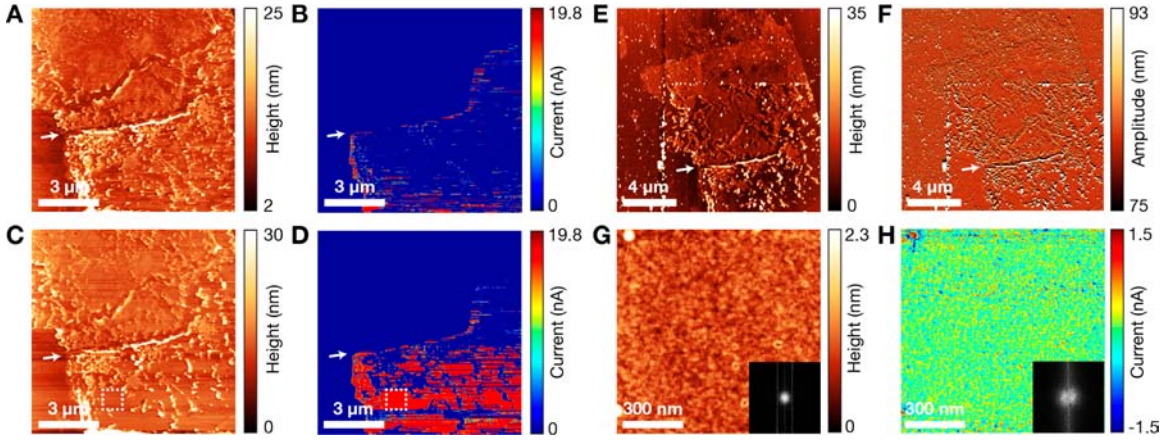

Figure 5. Structural and electronic changes from topographic and conducting AFM imaging. (A) Topographic contact mode AFM image of the functionalized bilayer graphene sample region marked in the white dotted square in Figure 2B. A crack in the bilayer graphene flake is marked at the white arrow. The region of the sample below the crack is contacted by an electrode, but the region above the crack is not. (B) Current image acquired simultaneously with (A). (C) Topographic and (D) current images of the same region as (A) and (B) after several more scans. The region below the crack shows increasing current where a noncovalently attached layer has been cleaned away by imaging. Applied sample voltage in (A)−(D) was 0.4 V. (E) Topographic noncontact mode AFM image and (F) phase image at a higher magnification than images (A)−(D). The same crack in the sample is indicated at the white arrow. Residue that was pushed aside during imaging earlier is visible as a vertical and horizontal line. (G) Topographic and (H) current images from the region in the white dashed square in (C) and (D) at applied sample bias of 0.1 V. The insets show the 2D fast Fourier transforms (FFTs) of each image, which suggest that the degree of inhomogeneity in the topography and current do not match.

observed for the G peaks, a likely indication of increased doping at the edges.

A more noticeable change is observed in the FWHMs, where the $2D_{22}$ and $2D_{21}$ peaks broaden with increasing covalent functionalization and the $2D_{12}$ and $2D_{11}$ peaks stay constant. Under noncovalent functionalization alone, there is little noticeable change in the peak widths. The two components that show the significant broadening with covalent functionalization correspond to the DR transitions with electronic excitation from the lower valence band to the upper conduction band. The broadening of these peaks appears to be a key indicator of covalent functionalization and has not been reported previously to the best of our knowledge. The contrast in the FWHM of the $2D_{22}$ peak is visually seen in the spatial map of Figure 4E. Finally, the intensities of the 2D peak components are shown to decrease for the $2D_{12}$ and $2D_{11}$ but stay nearly constant for the $2D_{22}$ and $2D_{21}$, the opposite of the indicators in width. In monolayer graphene, the 2D intensity decreases with increasing doping,[55,56] and a similar trend has been observed for bilayer graphene.[54] We note that the 2D peak intensity decreases for both covalent and noncovalent functionalization. For noncovalent functionalization, p-doping occurs due to physisorption of electron-withdrawing groups. The covalent diazonium functionalization is also effectively p-doping because it requires electron transfer out of the graphene for initially forming the aryl radical.[6] The DR transitions that correspond to doping are from the upper valence band to the lower conduction band. It appears that the $2D_{12}$ and $2D_{11}$ intensities are good indicators of doping, whereas the $2D_{22}$ and $2D_{21}$ widths are good indicators of disorder. The spatial map of the total 2D/G intensity ratio is shown in Figure 4F and shows a strong contrast between the covalent and noncovalently functionalized regions, as well as contrast between the edges and centers of the flake.

Conductive Atomic Force Microscopy (AFM). Topographic and conductive atomic force microscopy (AFM) images are shown in Figure 5 to illustrate the evolution of the structural and electronic properties of the bilayer graphene after functionalization. The same area of the sample mapped with Raman spectroscopy in Figures 2−4 was imaged here, again, to show the contrast between the portion of the sample that is connected to the electrodes and the portion that is not. In all the topographic AFM images shown here, the bilayer flake is higher than the SiO_2 background region by approximately 2−3 nm. However, the typical height of monolayer graphene on SiO_2 in AFM is ∼1 nm due to adsorbed water below or above the graphene flake, and the interlayer height in graphite is 0.335 nm, so the height we measure suggests that there is an additional layer of material. The most likely explanation is a combination of organic residues from photolithography and physisorbed species from the noncovalent contribution in the diazonium functionalization. There is also significantly more roughness than would be seen in pristine, unfunctionalized graphene (see ref 57 for additional information on the roughness of pristine graphene). Additional AFM images of another functionalized bilayer sample are shown in the Supporting Information, Figure S5, which show a similar increase in height and increase in roughness. The increase in height for graphene after diazonium functionalization has been reported previously by Koehler et al.,[32] and the presence of physisorbed layers has also been reported by Hossain et al.[34] and by Farmer et al.[33]

In the topographic image in Figure 5A, which approximately corresponds to the same area as the Raman maps in Figures 2−4, we can clearly see the crack in the sample, as indicated by the white arrow. The conductive AFM (cAFM) current image acquired simultaneously is shown in Figure 5B. Because the lower portion of the bilayer graphene is connected to the Ti/Au contact, which is held at ground while the tip is biased, we can see no current in the disconnected region above the crack and only some current in the connected region below the crack. However, the physisorbed residues seem to be impeding conduction except at the edges of the region. After several more scans, the amount of current in Figure 5D is significantly

dx.doi.org/10.1021/ja4083914 | J. Am. Chem. Soc. 2013, 135, 18866−18875

higher, with much of the region below the crack now showing high conduction. The corresponding topographic image in Figure 5C also shows that the patches of the sample where the current has increased are also smoother and lower in height, with the root mean square (RMS) roughness decreasing in the conductive patches from 2.3 to 0.8 nm. In contrast, the region above the crack maintains a very similar topography after several images. This observation strongly suggests that the AFM imaging has changed the sample by removing the nonconducting organic layer. The fact that the cleaning of the graphene is stronger in the electrically connected portion of the sample suggests that the electrical connection plays a role, perhaps via a joule heating mechanism that enhances the removal of material. The left-to-right and right-to-left scan direction images of Figure 5D are compared in the Supporting Information, Figure S4, and show streaks where the current is disrupted by the sweeping of physisorbed material.

A previous report of mechanical cleaning of bilayer graphene with contact mode AFM showed that residues from lithography can be pushed aside and improve the transport properties of the graphene device.[58] We believe that in our case, we also have a contribution due to current annealing or joule heating in the electrically connected portion of the sample, leading to even more cleaning. In addition, it is possible that the physisorbed material from the diazonium functionalization behaves differently under AFM imaging than lithography residues. Further evidence of the cleaning effect is shown in the tapping mode (noncontact) AFM images of Figures 5E and F, which are the height and phase images, respectively. These images show a larger region of the sample, and we can observe horizontal and vertical lines where the residues were pushed to the edges of the region where Figures 5A–D were obtained.

Finally, high-resolution topographic and current images (Figures 5G and H, respectively) from the center of the electrically connected region of the sample (in the regions marked by the small dashed squares in Figures 5C and D) were obtained after the previous cleaning steps. The topography of this region shows a spatial nonuniformity with RMS roughness of 0.2 nm, which is likely due to the roughness of the underlying SiO_2 substrate (which has a similar roughness). The corresponding current image, however, has a spatial nonuniformity that does not match the spatial frequency of the topographic image. That is, the topographic roughness does not influence and does not reflect the inhomogeneity in current. The difference in the spatial inhomogeneity between the topography and current images is illustrated by the 2D fast Fourier transforms (FFTs) in the insets of Figures 5G and H. Both FFTs show a generally disordered circular feature, but the FFT of the current is more broadly spread, indicating that there are more high-frequency contributions in the current image. We believe that this suggests the conductive nonuniformity arises from a nonuniform spatial distribution of covalent functionalization, as well as the possible formation of "patches" of higher and lower functionalization. The earlier work of Hossain et al. observed at an atomic level that covalent functionalization occurs at random positions on the graphene lattice rather than an in ordered manner.[34]

CONCLUSIONS

In conclusion, we have studied the covalent and noncovalent organic functionalization of bilayer graphene in an electrochemical reaction scheme with aryl diazonium salts and showed the characteristic changes that occur in the Raman spectra and conductive AFM. We observe changes in the G peak, which splits into G^+ and G^- components whose relative positions and intensities change with the degree of functionalization, reflecting changes in the effective electric field perpendicular to the bilayer graphene surface as well as the presence of disorder, particularly in the broadening of the G^+ peak. Changes in the 2D peak indicate the effects of both doping and disorder. In particular, the broadening of the $2D_{22}$ and $2D_{21}$ components indicates covalent functionalization, whereas the decrease in intensity of the $2D_{11}$ and $2D_{12}$ peaks corresponds to doping. AFM images show that the noncovalent portions of the functionalization can be removed from the bilayer surface with a combination of mechanical cleaning and current annealing and that the covalently functionalized region is spatially inhomogeneous in its conductivity.

METHODS AND MATERIALS

Sample Preparation. Bilayer graphene samples were prepared by mechanical exfoliation using adhesive tape onto heavily p-doped Si wafers capped with a 300 nm thick SiO_2 layer. Each bilayer flake was electrically contacted by patterning of source and drain contacts using photolithography and e-beam deposition of Ti (25 nm) and Au (75 nm) for the electrodes.

Functionalization Reaction. The samples were functionalized in a 4-bromobenzene-diazonium (Sigma-Aldrich) solution in acetonitrile (20 mM concentration), which was deposited onto the samples in a small droplet. The source and drain contacts were held at ground, and a positive reaction voltage was applied to a third tungsten probe inserted into the diazonium solution droplet (reaction voltages were 1.0, 1.25, and 1.5 V during subsequent reaction steps as indicated in the main text).

Characterization. The bilayer graphene samples were characterized before and after chemical functionalization by Raman spectroscopy using a Horiba LabRAM HR800 system and 100X objective lens. Laser excitation sources at 532 and 633 nm were used. Raman maps were collected using a motorized X-Y stage.

The AFM imaging was conducted on an Asylum MFP-3D system. Tapping (noncontact) mode imaging used Olympus OMCL-AC240TS probes, and contact mode and conductive imaging used the ORCA conductive module from Asylum and PtIr-coated probes from Bruker. During conductive AFM, the conductive tip is held at ground while the bias voltage was applied to the sample at the deposited Ti/Au contacts, and the imaging was conducted in contact mode. AFM images were analyzed and plotted using the Gwyddion software package,[59] which was also used to calculate the 2D fast Fourier transforms and root mean square roughness values.

ASSOCIATED CONTENT

Supporting Information

Additional Raman data (spatial maps of all 2D peak parameters, spectra taken at 532 nm laser excitation), peak fitting and confidence intervals for the 2D peaks, and additional conductive AFM images. This material is available free of charge via the Internet at http://pubs.acs.org.

AUTHOR INFORMATION

Corresponding Author

M. S. Strano. E-mail: strano@mit.edu

Notes

The authors declare no competing financial interest.

ACKNOWLEDGMENTS

This work was supported in part by the MRSEC Program of the National Science Foundation under award number DMR-0819762, with funding from the 2009 U.S. Office of Naval

Research Multi University Research Initiative (ONR-MURI) on Graphene Advanced Terahertz Engineering (GATE) at MIT, Harvard, and Boston University. M.S.S. is also grateful for a 2008 Young Investigator Program Award (YIP) from the U.S. Office of Naval Research. C.J.S. is grateful for partial financial support from the Chyn Duog Shiah Memorial Fellowship awarded by Massachusetts Institute of Technology. Device fabrication was conducted at the Harvard Center for Nanoscale Systems (CNS). Raman spectroscopy was partly conducted at the MIT Institute for Soldier Nanotechnologies (ISN). Useful discussions with D. Nida at ARL—Natick are acknowledged.

REFERENCES

(1) Geim, A. K. *Science* **2009**, *324*, 1530.
(2) Geim, A. K.; Novoselov, K. S. *Nat. Mater.* **2007**, *6*, 183.
(3) Loh, K. P.; Bao, Q.; Ang, P. K.; Yang, J. *J. Mater. Chem.* **2010**, *20*, 2277.
(4) Dreyer, D. R.; Park, S.; Bielawski, C. W.; Ruoff, R. S. *Chem. Soc. Rev.* **2010**, *39*, 228.
(5) Elias, D.; Nair, R.; Mohiuddin, T.; Morozov, S.; Blake, P.; Halsall, M.; Ferrari, A.; Boukhvalov, D.; Katsnelson, M.; Geim, A. *Science* **2009**, *323*, 610.
(6) Paulus, G. L. C.; Wang, Q. H.; Strano, M. S. *Acc. Chem. Res.* **2012**, *46*, 160.
(7) Niyogi, S.; Bekyarova, E.; Itkis, M. E.; Zhang, H.; Shepperd, K.; Hicks, J.; Sprinkle, M.; Berger, C.; Lau, C. N.; deHeer, W. A.; Conrad, E. H.; Haddon, R. C. *Nano Lett.* **2010**, *10*, 4061.
(8) Georgakilas, V.; Otyepka, M.; Bourlinos, A. B.; Chandra, V.; Kim, N.; Kemp, K. C.; Hobza, P.; Zboril, R.; Kim, K. S. *Chem. Rev.* **2012**, *112*, 6156.
(9) Wang, Q. H.; Hersam, M. C. *Nature Chem.* **2009**, *1*, 206.
(10) Jin, Z.; McNicholas, T. P.; Shih, C.-J.; Wang, Q. H.; Paulus, G. L. C.; Hilmer, A.; Shimizu, S.; Strano, M. S. *Chem. Mater.* **2011**, *23*, 3362.
(11) Ye, L.; Xiao, T.; Zhao, N.; Xu, H.; Xiao, Y.; Xu, J.; Xiong, Y.; Xu, W. *J. Mater. Chem.* **2012**, *22*, 16723.
(12) Sharma, R.; Baik, J. H.; Perera, C. J.; Strano, M. S. *Nano Lett.* **2010**, *10*, 398.
(13) Wang, Q. H.; Jin, Z.; Kim, K. K.; Hilmer, A. J.; Paulus, G. L. C.; Shih, C.-J.; Ham, M.-H.; Sanchez-Yamagishi, J. D.; Watanabe, K.; Taniguchi, T.; Kong, J.; Jarillo-Herrero, P.; Strano, M. S. *Nature Chem.* **2012**, *4*, 724.
(14) Morozov, S. V.; Novoselov, K. S.; Katsnelson, M. I.; Schedin, F.; Elias, D. C.; Jaszczak, J. A.; Geim, A. K. *Phys. Rev. Lett.* **2008**, *100*, 016602.
(15) Novoselov, K. S.; McCann, E.; Morozov, S. V.; Fal'ko, V. I.; Katsnelson, M. I.; Zeitler, U.; Jiang, D.; Schedin, F.; Geim, A. K. *Nat. Phys.* **2006**, *2*, 177.
(16) Ohta, T.; Bostwick, A.; Seyller, T.; Horn, K.; Rotenberg, E. *Science* **2006**, *313*, 951.
(17) Balog, R.; Jorgensen, B.; Nilsson, L.; Andersen, M.; Rienks, E.; Bianchi, M.; Fanetti, M.; Laegsgaard, E.; Baraldi, A.; Lizzit, S.; Sljivancanin, Z.; Besenbacher, F.; Hammer, B.; Pedersen, T. G.; Hofmann, P.; Hornekaer, L. *Nat. Mater.* **2010**, *9*, 315.
(18) Bekyarova, E.; Itkis, M. E.; Ramesh, P.; Berger, C.; Sprinkle, M.; de Heer, W. A.; Haddon, R. C. *J. Am. Chem. Soc.* **2009**, *131*, 1336.
(19) Shih, C.-J.; Wang, Q. H.; Jin, Z.; Paulus, G. L. C.; Blankschtein, D.; Jarillo-Herrero, P.; Strano, M. S. *Nano Lett.* **2013**, *13*, 809.
(20) Wang, X.; Ouyang, Y.; Li, X.; Wang, H.; Guo, J.; Dai, H. *Phys. Rev. Lett.* **2008**, *100*, 206803.
(21) Li, X.; Wang, X.; Zhang, L.; Lee, S.; Dai, H. *Science* **2008**, *319*, 1229.
(22) Han, M. Y.; Özyilmaz, B.; Zhang, Y.; Kim, P. *Phys. Rev. Lett.* **2007**, *98*, 206805.
(23) Bai, J.; Zhong, X.; Jiang, S.; Huang, Y.; Duan, X. *Nat. Nanotechnol.* **2010**, *5*, 190.
(24) Liang, X.; Jung, Y.-S.; Wu, S.; Ismach, A.; Olynick, D. L.; Cabrini, S.; Bokor, J. *Nano Lett.* **2010**, *10*, 2454.
(25) Özyilmaz, B.; Jarillo-Herrero, P.; Efetov, D.; Kim, P. *Appl. Phys. Lett.* **2007**, *91*, 192107.
(26) Schwierz, F. *Nat. Nanotechnol.* **2010**, *5*, 487.
(27) Wang, F.; Zhang, Y.; Tian, C.; Girit, C.; Zettl, A.; Crommie, M.; Shen, Y. R. *Science* **2008**, *320*, 206.
(28) Zhang, Y.; Tang, T.-T.; Girit, C.; Hao, Z.; Martin, M. C.; Zettl, A.; Crommie, M. F.; Shen, Y. R.; Wang, F. *Nature* **2009**, *459*, 820.
(29) Xia, F.; Farmer, D. B.; Lin, Y.-M.; Avouris, P. *Nano Lett.* **2010**, *10*, 715.
(30) Park, J.; Jo, S. B.; Yu, Y.-J.; Kim, Y.; Yang, J. W.; Lee, W. H.; Kim, H. H.; Hong, B. H.; Kim, P.; Cho, K.; Kim, K. S. *Adv. Mater.* **2012**, *24*, 407.
(31) Zhang, W.; Lin, C.-T.; Liu, K.-K.; Tite, T.; Su, C.-Y.; Chang, C.-H.; Lee, Y.-H.; Chu, C.-W.; Wei, K.-H.; Kuo, J.-L.; Li, L.-J. *ACS Nano* **2011**, *5*, 7517.
(32) Koehler, F. M.; Jacobsen, A.; Ensslin, K.; Stampfer, C.; Stark, W. J. *Small* **2010**, *6*, 1125.
(33) Farmer, D. B.; Golizadeh-Mojarad, R.; Perebeinos, V.; Lin, Y.-M.; Tulevski, G. S.; Tsang, J. C.; Avouris, P. *Nano Lett.* **2009**, *9*, 388.
(34) Hossain, M. Z.; Walsh, M. A.; Hersam, M. C. *J. Am. Chem. Soc.* **2010**, *132*, 15399.
(35) Ferrari, A. C.; Basko, D. M. *Nat. Nanotechnol.* **2013**, *8*, 235.
(36) Malard, L. M.; Pimenta, M. A.; Dresselhaus, G.; Dresselhaus, M. S. *Phys. Rep.* **2009**, *473*, 51.
(37) Yan, J.; Villarson, T.; Henriksen, E. A.; Kim, P.; Pinczuk, A. *Phys. Rev. B* **2009**, *80*, 241417.
(38) Bruna, M.; Borini, S. *Phys. Rev. B* **2010**, *81*, 125421.
(39) Mafra, D. L.; Gava, P.; Malard, L. M.; Borges, R. S.; Silva, G. G.; Leon, J. A.; Plentz, F.; Mauri, F.; Pimenta, M. A. *Carbon* **2012**, *50*, 3435.
(40) Thomsen, C.; Reich, S. *Phys. Rev. Lett.* **2000**, *85*, 5214.
(41) Saito, R.; Jorio, A.; Souza Filho, A. G.; Dresselhaus, G.; Dresselhaus, M. S.; Pimenta, M. A. *Phys. Rev. Lett.* **2001**, *88*, 027401.
(42) Malard, L. M.; Nilsson, J.; Elias, D. C.; Brant, J. C.; Plentz, F.; Alves, E. S.; Castro Neto, A. H.; Pimenta, M. A. *Phys. Rev. B* **2007**, *76*, 201401.
(43) Ferrari, A. C.; Meyer, J. C.; Scardaci, V.; Casiraghi, C.; Lazzeri, M.; Mauri, F.; Piscanec, S.; Jiang, D.; Novoselov, K. S.; Roth, S.; Geim, A. K. *Phys. Rev. Lett.* **2006**, *97*, 187401.
(44) Martins Ferreira, E. H.; Moutinho, M. V. O.; Stavale, F.; Lucchese, M. M.; Capaz, R. B.; Achete, C. A.; Jorio, A. *Phys. Rev. B* **2010**, *82*, 125429.
(45) Cançado, L. G.; Jorio, A.; Ferreira, E. H. M.; Stavale, F.; Achete, C. A.; Capaz, R. B.; Moutinho, M. V. O.; Lombardo, A.; Kulmala, T. S.; Ferrari, A. C. *Nano Lett.* **2011**, *11*, 3190.
(46) Gava, P.; Lazzeri, M.; Saitta, A. M.; Mauri, F. *Phys. Rev. B* **2009**, *80*, 155422.
(47) Lucchese, M. M.; Stavale, F.; Ferreira, E. H. M.; Vilani, C.; Moutinho, M. V. O.; Capaz, R. B.; Achete, C. A.; Jorio, A. *Carbon* **2010**, *48*, 1592.
(48) Pimenta, M. A.; Dresselhaus, G.; Dresselhaus, M. S.; Cancado, L. G.; Jorio, A.; Saito, R. *Phys. Chem. Chem. Phys.* **2007**, *9*, 1276.
(49) Ferrari, A. C. *Solid State Commun.* **2007**, *143*, 47.
(50) Lazzeri, M.; Mauri, F. *Phys. Rev. Lett.* **2006**, *97*, 266407.
(51) Pisana, S.; Lazzeri, M.; Casiraghi, C.; Novoselov, K. S.; Geim, A. K.; Ferrari, A. C.; Mauri, F. *Nat. Mater.* **2007**, *6*, 198.
(52) Das, A.; Pisana, S.; Chakraborty, B.; Piscanec, S.; Saha, S. K.; Waghmare, U. V.; Novoselov, K. S.; Krishnamurthy, H. R.; Geim, A. K.; Ferrari, A. C.; Sood, A. K. *Nat. Nanotechnol.* **2008**, *3*, 210.
(53) Malard, L. M.; Elias, D. C.; Alves, E. S.; Pimenta, M. A. *Phys. Rev. Lett.* **2008**, *101*, 257401.
(54) Das, A.; Chakraborty, B.; Piscanec, S.; Pisana, S.; Sood, A. K.; Ferrari, A. C. *Phys. Rev. B* **2009**, *79*, 155417.
(55) Casiraghi, C. *Phys. Rev. B* **2009**, *80*, 233407.
(56) Basko, D. M.; Piscanec, S.; Ferrari, A. C. *Phys. Rev. B* **2009**, *80*, 165413.
(57) Dean, C. R.; Young, A. F.; Meric, I.; Lee, C.; Wang, L.; Sorgenfrei, S.; Watanabe, K.; Taniguchi, T.; Kim, P.; Shepard, K. L.; Hone, J. *Nat. Nanotechnol.* **2010**, *5*, 722.

(58) Goossens, A. M.; Calado, V. E.; Barreiro, A.; Watanabe, K.; Taniguchi, T.; Vandersypen, L. M. K. *Appl. Phys. Lett.* **2012**, *100*, 073110.
(59) Nečas, D.; Klapetek, P. *Cent. Eur. J. Phys.* **2012**, *10*, 181.